Fusion Engineering and Design 215 (2025) 114947

Contents lists available at ScienceDirect

Fusion Engineering and Design

journal homepage: www.elsevier.com/locate/fusengdes

Maximum likelihood bolometric tomography for DTT diagnostic design

E. Peluso [a,b,*], T. Craciunescu [c], G.M. Apruzzese [a], A. Belpane [d], S. Palomba [e], L. Senni [f], V. D'Agostino [b], M. Gelfusa [b], P. Gaudio [b], L. Boncagni [a]

[a] ENEA, Nuclear Department, C.R. ENEA-Frascati, Via E. Fermi 45, 00044, Frascati RM, Italy
[b] Department of Industrial Engineering, University of Rome Tor Vergata, Via del Politecnico 1, 00133, Rome RM, Italy
[c] National Institute for Laser, Plasma and Radiation Physics, Magurele-Bucharest, Romania,
[d] Consorzio RFX (CNR, ENEA, INFN, Università di Padova, Acciaierie Venete SpA), Corso Stati, Padova, 35127, Italy
[e] DTT S.C.a r.l., Via E. Fermi 45, I-00044, Frascati RM, Italy
[f] CNR - Institute for applied mathematics 'Mauro Picone' (IAC)Via dei Taurini, 19, 00185 Roma Italy

A R T I C L E I N F O

Keywords:
DTT
Bolometry
Tomography
Nuclear fusion
Tokamak
Synthetic diagnostic

A B S T R A C T

On both the Joint European Torus (JET) and the ASDEX-Upgrade (AUG) tokamaks, an Expectation Maximization algorithm has been adapted to implement a Maximum Likelihood (ML) approach to derive tomograms from bolometers data. The main feature of such an approach is the ability to estimate the variance associated with the reconstructed tomograms and hence the uncertainties in the derived quantities. It has therefore been selected to support the design of the bolometric diagnostics for the Divertor Tokamak Test Facility (DTT). A reliable reconstruction of the emissivity profile is indeed relevant for the scientific exploitation of the device. As any tomographic inversion method is an ill-conditioned problem, two milestones should be achieved: ensuring the reconstruction of specific features and minimizing the risk of producing artefacts. The design strategy for the bolometric diagnostic on DTT involves testing various possible layouts to ensure that they meet the above requirements and are compatible with the engineering and machine constraints. This contribution focuses on showing how the conceptual bolometric layout can handle different phantoms mimicking typical emissivities observed on JET and AUG. A methodology has been developed to further optimize the layout within the constraints of the machine design. For the initial phase of DTT, a reduced layout is proposed, utilizing half of the conceptual lines of sight. The ability to reconstruct specific emissivity features while minimizing the risk of producing artefacts has been tested. The current ML implementation uses an anisotropic diffusion technique and is already significantly faster than the JET implementation for each reconstruction.

1. Introduction

Defining the layout of a line-integrated diagnostic involves several steps before it can be finalized. These steps include determining specific locations and access points to the plasma, as well as selecting the most suitable type of detectors, which may require a customized active cooling system. Finally, budgetary constraints must also be taken into account. To speed up the process, the bulk of a synthetic diagnostic needs to be established. Plasma diagnostics can be used either for scientific exploitation of the data collected and/or for feedback and feed-forward control of the plasma discharge. Bolometry can be used for both. Bolometers are nowadays routinely used in magnetically confined plasma devices to measure the widest possible range of the electromagnetic spectrum, assuming an optically thin plasma[1]. They provide a passive diagnostic that can be used to retrieve important time dependent physical quantities of the plasma [2], and their application includes: a) power balance; b) magneto-hydrodynamics (MHD) instabilities; c) impurity screening, transport and localization; d) modelling. Most studies in these fields can be conducted once a reliable estimate of the poloidal emissivity profile is obtained. This is achieved by solving an ill-posed and inverse problem known as tomography. Once a tomogram is obtained, the radiated power at different locations of the device, as well as the radiation and the radiation density profiles can be derived.

At the same time, as mentioned above, each bolometer collects time-dependent line-integrated measurements. These measurements are becoming increasingly important as indicators of specific phenomena that are not yet fully understood and therefore cannot yet be prevented,

* Corresponding author.
E-mail address: emmanuele.peluso@uniroma2.it (E. Peluso).

https://doi.org/10.1016/j.fusengdes.2025.114947
Received 5 December 2024; Received in revised form 26 February 2025; Accepted 7 March 2025
Available online 25 March 2025

and whose occurrence can significantly impact the plasma evolution and even the operational safety of the device. In fact, bolometric measurements can be used for feedforward and even feedback plasma control. This is a trend that has emerged in the last decade in order to achieve ITER and DEMO requirements and advanced plasma conditions, including the control and monitoring of dangerous plasma instabilities such as Multifaceted Asymmetric Radiations From the Edge (MARFEs) and MHD related ones. For example, a series of observations related to the unstable evolution of the X-point radiator regime [3], i.e. a MARFE [4], have led it to be strictly related to disruptive behaviours, independently on the species used for impurities seedings and on the wall type, e.g. Berillium (Be) at JET or Tungsten (W) on AUG [5]. Similarly, the growth and dynamics of Tearing Modes (TM) instabilities have quite recently been linked to impurity fluxes and their accumulation either in the core or in the edge[6,7],. In terms of operational control then, AUG has demonstrated a methodology for tracking disruptive paths leading to the so called “density limit disruptions", which are still related to MARFEs [8]. In all the aforementioned cases bolometry play an important role.

In addition to a series of geometric constraints, such as the integration with other diagnostics, operational systems, remote handling, and the actual available physical space, the design of the bolometric diagnostic requires to maximize the coverage of the poloidal plane within the available budget. It must then be verified that the hypothetical Line of Sights (LoS) layout can both retrieve the emissivity profiles with a limited risk of producing artifacts and be suitable for real time operational purposes [9]. The facility under construction at the ENEA research centre in Frascati, the Divertor Tokamak Test facility (DTT)[10], is designed to achieve reactor relevant parameters [11], comparable with ITER and DEMO.

The bolometric diagnostic [11-13], has indeed been classified as “essential” for DTT and will therefore be available from the first plasma of DTT.

The structure of this paper is as follows. Section 2 recalls the actual layout of the bolometric diagnostic for DTT [13], including a brief review of the bolometers considered for its design at this stage. At the same time, a possible alternative reduced layout is also proposed. To validate the layouts shown in Section 2, Section 3 reports the main features of the tomographic algorithm chosen: an Expectation and Maximization one, based on the Maximum Likelihood (ML) approach[14]. Section 4 describes the synthetic diagnostic developed to validate the layout as well as the results obtained by using the ML approach on synthetic data. Finally, Section 5 presents the conclusion regarding the contribution.

2. DTT bolometric layout

The modern concepts of metal foil bolometers for measuring the total radiated power from an optically thin plasma can be rooted back to [1], where the basic idea of measuring the incident radiated power on a gold foil bolometer being one of the four resistances of a Wheatstone bridge is presented.

As mentioned above, the DTT environment is expected to be quite a challenging one, with 0.5 $MW\ m^{-2}$ of expected incident radiated power flux. An accurate choice of the bolometers for DTT needs to be considered, and at this stage metal foil bolometers appear to be the most reliable detector choice [13], having been customized and installed almost every modern TOKAMAKs, such as JET[15] (in decommissioning), AUG[16] and EAST[17] for example.

A detailed discussion regarding the mechanical layout and its behaviour with respect to the mentioned high incident thermal load is beyond the scope of this article. More details can be found in [18]. It should be noted in any case that alternatives to commercial bolometers are also being considered at this stage. The prototypes currently under development for ITER [19,20], have demonstrated noteworthy properties that could streamline engineering solutions for an application on DTT, enhancing the operational safety of the device by reducing the need to cool the structures housing the bolometer heads for instance.

SubSection 2.1 provides a brief description of the bolometric layout [13] with 216 Lines of Sights (LoS), hereafter referred to as the *extended* one, and a *reduced* one with 120 LoS described in this article; both completely cover a poloidal section of the plasma.

2.1. Conceptual diagnostic full layout and reduced one

The preliminary conceptual design with 216 LoS has been completed and is based on commercial bolometers[13]. All of them will be housed in the same sector (#15), in different ports (P) numbered from 1 to 4, (e.g. P1, P2, P3, P4) so as not to break the toroidal symmetry of the measurements [21], there is no gas puffing toroidally located between any of the arrays. At this stage, each set of bolometer heads is cooled and housed in a support box unit which is also actively cooled[22,18]; such box has been designed to have a pinhole for the bolometer array. Efforts are currently underway to define the millimetric layer grid to prevent ECRH stray radiation from interfering with the bolometric measurements, as well as other engineering solutions to reduce further the stray radiation and the reflections to negligible levels. More details are given in Section 4. It is also important to state that significant efforts are

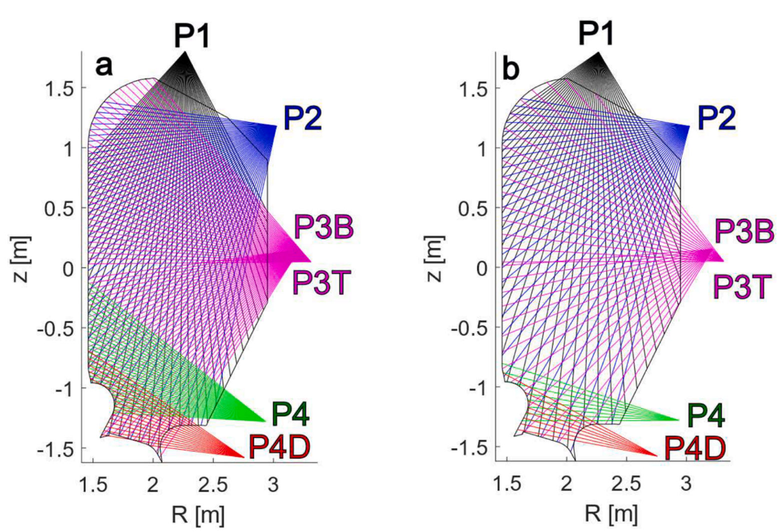

Fig. 1. a) Suggested layout with 216 LoSs [13]; b) reduced layout with 120 LoS. The letter P stands for “port” and since the sector housing the bolometers has four ports available, the number stands for the number of the port. The final letter has been used to discriminate different arrays in the same port.

Table 1
LoSs number for both the considered layouts.

Bolometer camera array	216 layout: # LoS	120 layout: # LoS
P1	48	40
P2	48	32
P3 Top (P3T)	36	16
Port 3 Bottom [P3B]	36	16
Port 4 (P4)	32	8
Port 4 Divertor [P4D]	16	8

currently being made to integrate different systems and diagnostics already in this design phase of the device, and therefore it cannot be excluded a priori a future need to adapt the bolometric layout and support unit, for example, by using different solutions such as in ITER for the divertor [23]

The conceptual design with 216 LoSs is shown in Fig. 1a. The Fig. 1b instead shows the reduced set with 120 LoSs, which has also been studied to check the actual feasibility of reducing the number of LoSs, especially for the first plasma and for the so called “phase1” of the device. Such a reduced number of LoSs has been the result of a feasibility study aimed at maximizing the poloidal coverage of the plasma without increasing more than roughly a ~50 % the maxima widths of equivalent LoS. In principle, the layout could still be adjusted based on further requirements from other systems with higher priorities, such as remote handling or plasma operations, as well as to achieve a better coverage of the plasma regions in advanced scenarios. The methodology, based on the bulk of the synthetic diagnostic described in this article, will allow to easily tune and test any possible change in the layout in any case.

Table 1 provides the number of the considered LoSs for both layouts. Fig. 2 provides the coordinates, (p,ϕ), of the points lying on each LoS at the minimum distance with respect to the major radius of the device, both for the extended and the reduced layouts [24]. The parameter “p” is usually referred as the impact parameter and the angle “ϕ” can be read then as the angle that a perpendicular line to the LoS, which then passes through the major radius of the device, forms with the radial axis

It is important to note that the reduced layout has been derived by varying: the focal distance between the bolometers and the pinholes; the distance, along the same arc, between bolometers; eventually, the position of the first bolometer.

This methodology allowed to reduce the number of bolometers to be used and therefore, the number of LoSs.

The sinogram in Fig. 2b shows how the reduced layout actually improves the poloidal coverage of the extended one, by considering for example the improvement of the vertical array from the port 1 (P1) looking at the inner guard wall limiter on the inner top side of the device which could in principle be a critical point for radiation control [8]. It should be noted that the coverage of such an area (inner top limiter close to the inner guard one) can in principle be achieved with 216 LoS, using the above methodology, and thus landing on a different extended layout. Looking again at Fig. 2b, it can be observed that also the horizontal coverage of the LoSs is slightly more optimised compared to the extended case.

For the sake of completeness, such a description of the LoSs is a complete one; indeed, by considering the region of the (p,ϕ) less covered by the actual layouts, i.e. the one with negative absolute distance ($p \in [-\max(p), 0]$) and therefore rather small poloidal aperture ($\phi \in [0, 1]rad$), it becomes clear that such LoSs cannot be considered at this stage due to engineering constraints: they would correspond to LoSs looking at the divertor, passing through the plasma, and starting from the top of the inner wall close to the inner guard limiter.

The next section provides a brief overview of the inversion algorithm used for the bolometric tomography, which has already been widely applied and improved on JET[25] and also implemented on AUG[26].

3. Short overview of the maximum likelihood approach

The layouts presented in the previous section need to be benchmarked with synthetic emissivity profiles, usually referred as *phantoms*, to verify their real ability to reproduce specific features while minimizing the possibility to producing artefacts, once an inverse algorithm is applied to the collected data.

An Expectation Maximization (EM) algorithm based on a Maximum Likelihood (ML) approach is used to perform such a task. It was first used for neutron and gamma tomography on JET[27] and later on bolometric data both on JET[25] and then with further implementations, on AUG [26].

The ML approach is well established in the literature as well as its implementation [28-31], and represents a specific type of Computerized Tomography (CT). The measurements $\boldsymbol{g}$ and the emission process are classically assumed to follow Poissonian distributions; however such a hypothesis can be relaxed allowing also non-Poissonian probability distribution functions (pdfs) to be considered, as already demonstrated on JET, AUG and reported in the literature[14,25,26],. The ML starts from the need to maximize the following likelihood (L) :

$$L(g|f) = \prod_m \frac{1}{g_m!}(\overline{g_m})^{g_m} \times exp(-\overline{g_m}) \tag{1}$$

Where $\overline{g_m} = E\{g_m|\boldsymbol{f}\}$ represents the statistically expected conditioned value of the measurement value g_m, by assuming an emissivity profile $\boldsymbol{f}$ composed by “n” pixels, i.e. the poloidal section of each actual three-dimensional voxel. The ML is then coded by an EM algorithm which provides an estimate $\boldsymbol{f}_{\mathbf{ML}}^{(\mathbf{k}^*)}$ of $\boldsymbol{f}$. The core of the code is based on matrices computations, e.g. [30]. By following the same notations then as in [30]

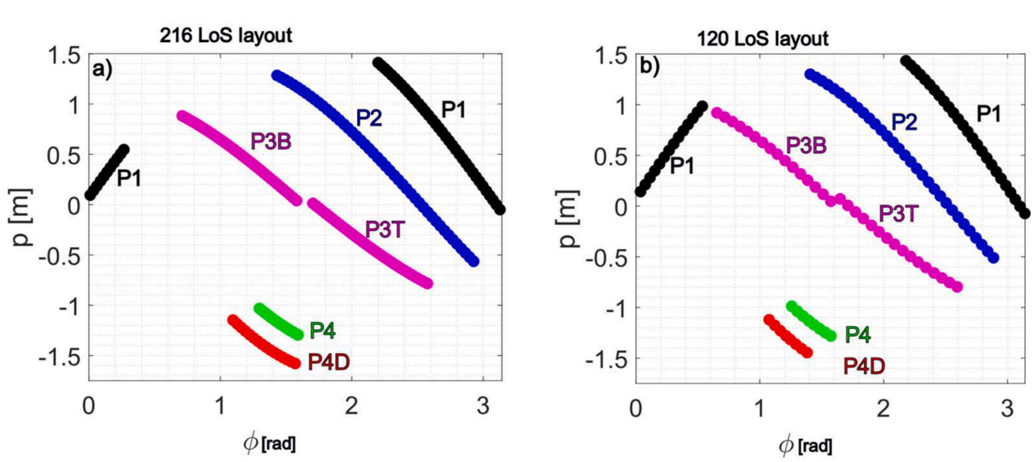

Fig. 2. Sinograms reporting only the impact parameters p and the corresponding angle ϕ for the extended layout a) and for the reduced layout b).

the following eq.(2) holds. Please note that from now on, the Einstein notation has been used.

$$\overline{g_m} = H_{mn} f^n \quad (2)$$

In general, it is possible to estimate the projection matrix $\boldsymbol{H}$ by knowing the geometry of the diagnostic.

The details regarding the evaluation of such matrix, describing the optical contribution of each voxel, are provided in subSection 4.1. The iterative procedure can be summarized as follows:

$$f_n^{(k+1)} = \frac{f_n^{(k)}}{\sum_m H_{mn}} \left(g_m \Big/ H_{mj} f^{j,(k)} \right) H_n^m \quad (3)$$

Once a convergence criterion is satisfied [29], the emissivity at the landing step k^* is considered, i.e. $\boldsymbol{f} = \boldsymbol{f}_{\mathbf{ML}}^{(\mathbf{k}^*)}$. The ML approach has the advantages of having a matrix based and well established iterative procedure for retrieving both the emissivity $\boldsymbol{f}_{\mathbf{ML}}^{(\mathbf{k}^*)}$ and covariance matrix $\boldsymbol{K}_{\mathbf{ML}}^{(\mathbf{k}^*)}$, i.e. the uncertainty on the estimate of the emissivity $\boldsymbol{f}_{\mathbf{ML}}^{(\mathbf{k}^*)}$ for each voxel [25,30],. An important feature of the variance estimates lies in the fact that $\boldsymbol{K}_{\mathbf{ML}}^{(\mathbf{k}^*)}$, i.e. the image of the uncertainties for the emissivity pattern obtained $\boldsymbol{f}_{\mathbf{ML}}^{(\mathbf{k}^*)}$, resembles the profile itself. This is in contrast with linear reconstruction methods where bright features contribute to distant and low intensity regions [30].

It has to be stated that the ignorance of the true statistical nature of the phenomenon is not a real limitation [25,26,32], for the EM algorithm. It only leads to a worse than optimal reconstruction [14,29],. The more "Poissonian" the statistical nature of the phenomenon is, the better the algorithm works.

The implemented algorithm follows the approach adopted for AUG with regard to a further regularization procedure. An anisotropic smoothing technique is applied by using a tensor-driven partial differential equation (PDE) method. The tensor considered is a specific form of the so-called diffusion tensor, derived from the poloidal magnetic flux topology. A diffusion PDE smoothing, based on a Line Integral Convolution approach along different directions, i.e. different curvature constraints, is then driven by the diffusion tensor itself [26,33],.

To conclude the section then, the potential application of machine learning algorithms for the purpose of inferring free parameters, a process referred to as "model calibration," is currently under consideration [34]. However, the implementation of such an algorithm is not a simple task, nor it is likely to be feasible in any cases for such application. Indeed, for a bolometric application in fact, the cost function should be based only on the goodness of the match between synthetic and the reconstructed brightness profiles. However, being the problem ill-posed, more solutions with different sets of parameters could provide compatible back-calculated projections and different tomograms. An alternative approach should be adopted, based on testing several synthetic emissivity profiles. Then, for a more extended applications, further methodologies should be applied that are currently either under development [9] or have already been applied on other devices [35]. In any case, as a general approach, the regularization along the regions located on the same isopoloidal flux curves is much greater than the one perpendicular to it [26]. Such a choice can been justified in many way, such as the theoretical and empirical evidence of a parallel thermal conductivity being much greater than the perpendicular one for example.

Once the main features of the algorithm have been recalled, the following section describes the results obtained to validate the present extended and *reduced* layout configurations.

4. Synthetic diagnostic layout validation

This section consists of two subsections. SubSection 4.1 is devoted to describe the main features of the synthetic diagnostic that has been realized. SubSection 4.2 presents the main results of the validation of the bolometric layout and of its first reduced configuration.

4.1. Definition of the bulk synthetic diagnostic

While the description of the mechanical layout is beyond the scope of this contribution (the actual layout has only been described in general terms in sub-Section 2.1.), it must be mentioned that several innovative solutions have been adopted [18,22],.

Once the actual space available in each of the four ports of the dedicated sector, i.e. P1, P2, P3, P4, had been estimated, it has been possible to define a synthetic diagnostic starting from two constraints and one parameter for the geometry. The constraints are: a) the centre of the pinhole; b) the maximum spatial excursion of the arc; the parameter is then: c) the position, i.e. the dimensions of the first bolometric head.

The above constraints have been used to define the poloidal coverage of each bolometer array in order to optimize the poloidal aperture of the pinhole on a given image plane both to minimize the overlap of adjacent equivalent LoSs and to allow for a possible reduced layout of the bolometric system. By considering a shifted frame of reference with origin on the equatorial plane of the torus and in the centre of the central solenoid, i.e. $O \equiv (R, z) \equiv (0, 0)$ the following image planes have been used: a) $z = 0$ for P1; b) $R = 2.19m$ for both P2 and P3B and P3T; c) $R = 1.64\ m$ for both P4 and P4D.

The second step in defining the bulk of the synthetic diagnostic is to estimate the expected brightness of each bolometer. This has been possible by evaluating the contribution of each voxel within the

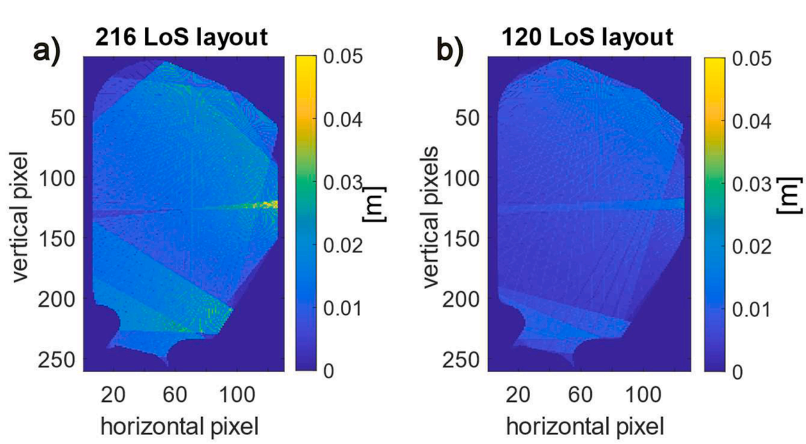

Fig. 3. Cumulative sum of the projection matrices H for the extended (a) and reduced layouts (b), once the poloidal aperture of the pinhole on the cooled box housing the bolometers has been optimized on each port to avoid the overlap of the LoS, and once truncated pyramidal cones have been considered for each chord. The brighter a pixel, the higher its contribution on the overall reconstruction.

truncated pyramidal representation of a LoS. For the geometry of the layouts considered, analytical estimates are possible. Although it would also be possible to estimate the evaluation of such contributions, as well as the etendues, using dedicated software such as CHERAB [36], it should also be noted that in the latter case, for focal lengths of the order of those in play, the analytical estimates are not expected to be far from the raytraced ones [37], as well as for the former, by taking into account the actual poloidal and toroidal extension of each line of sight, any difference is not expected to play a relevant role on the estimates. With respect to the raytracing, it is in fact more relevant to study the effect of non-trivial sources of error such as the thermal effects on the structures, for which further studies are ongoing[22].

The absorbed power from a bolometer, P_m, of an array having *″m″* LoSs, such as 48 for the one located in P1 (see Table 1) for example, can be expressed as:

$$P_m = \frac{E_m}{4\pi}\int_{l_m} \varepsilon\, dl = \frac{E_m}{4\pi} I_m \tag{4}$$

Where the aforementioned integral extends over each LoS l_m, E_m stands for the etendue of the bolometer foil “m” which also accounts also for the portion of the solid angle that the detector must cover to observe the voxels within its cone of view; ε stands for the emissivity profile, and I_m for the line integrated emissivity detected, i.e. the brightness of the LoS. On the other hand, considering a grid of n pixels, (33,800 for the one considered here), corresponding to a poloidal pixel resolution of A_{pix} $= 1.56$ cm^2. The same line of integral can be written as:

$$I_m = H_{mp}\varepsilon^p = \frac{4\pi\left(\varepsilon_m^p d\Omega_p dV_p\right)}{E_m} \tag{5}$$

Where $\boldsymbol{H}$ is the projection matrix described in Section 3, $d\Omega$ is the portion of the solid angle the voxel uses to see the detector and $dV_p = 2A_{pix}h_{\phi,p}$ stands for the parallelepipedal element of volume, having poloidal section defined as A_{pix} and half toroidal width $h_{\phi,p}$.

Such element of volume has been deliberately chosen to describe the voxel “p”, for which, the farther it is from the detector, the wider $h_{\phi,p}$ is. The line integral is naturally the sum of the contributions from different voxels composing the LoS. By doing so, the following can be obtained:

$$H_{mp} = \frac{2A_{pix}A_{foil}}{E_m}\left(\frac{h_{\phi,foil}}{d}\right)\left(\frac{1}{l_p}\right) \tag{6}$$

Where “d” stands for the distance from the centre of the active foil to the centre of the pinhole; $h_{\phi,foil}$ is half of the toroidal aperture of the pinhole; A_{foil} stands for the active area of the foil bolometer, and l_p is the distance of the centre of the sensible foil to the centre of the poloidal projection of the voxel considered, i.e. the pixel with area A_{pix}. By doing so the projection matrices have been obtained for both layouts.

In principle, reflections and ECRH stray radiation could concur to the measured brightness of a detector. Regarding the former aspect, the reflectivity of the materials of the support structure hosting the bolometers is rather low in the spectral range of greatest interest for

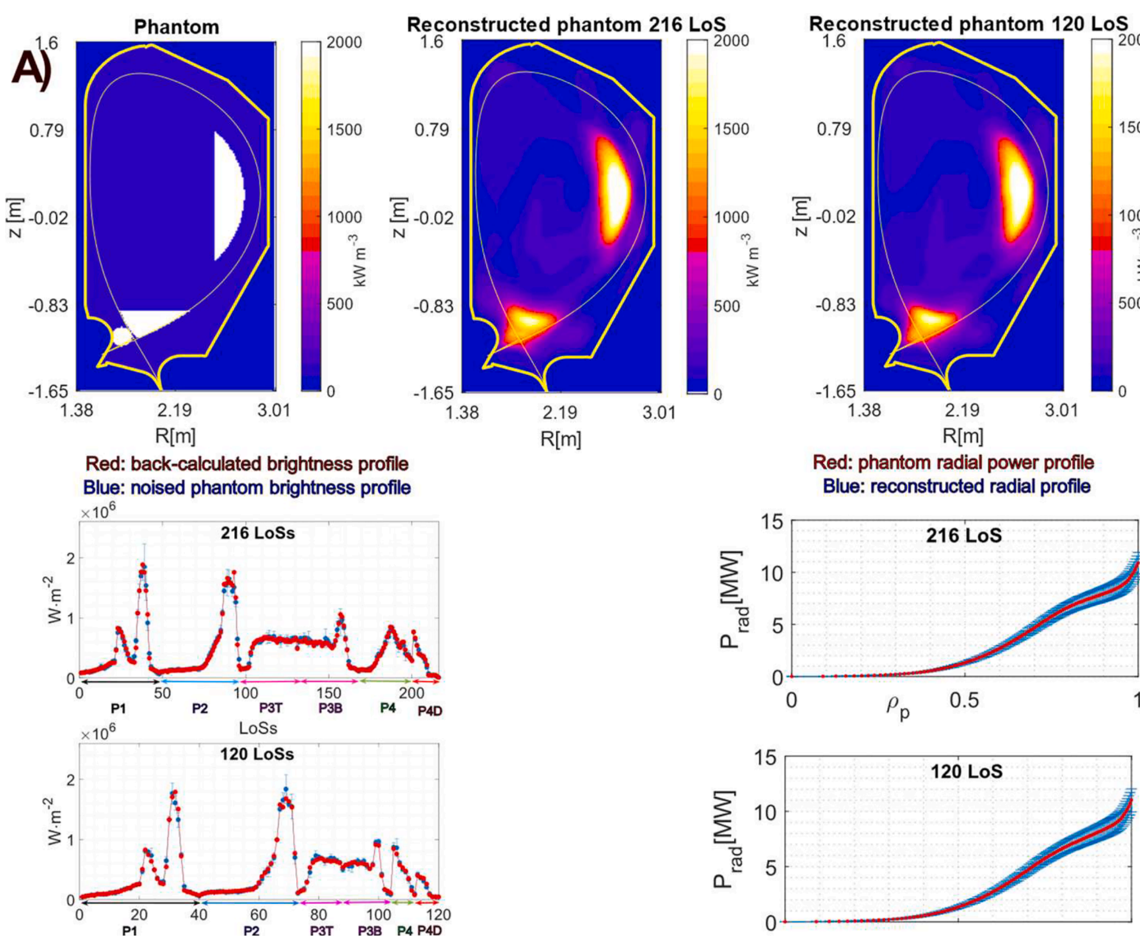

Fig. 4. First phantom studied, reporting an emissivity profile for a Single Null configuration. a) Inner detached and X-point radiator with impurities accumulating close to the edge. The first row on top shows, from left to right, the created phantom, the reconstructed one using the extended layout (216 LoS) and the one obtained with the reduced one (120 LoS). Second row on the bottom shows, from left to right: the synthetic normally noised brightness profile of the bolometers for the map of emissivity of the phantom (blue) and the back calculated brightness profile (red) for each detector, for both layouts; the radiation profiles up to the LCFS. The error bars are related to the 10 % of normally noised set of projections.

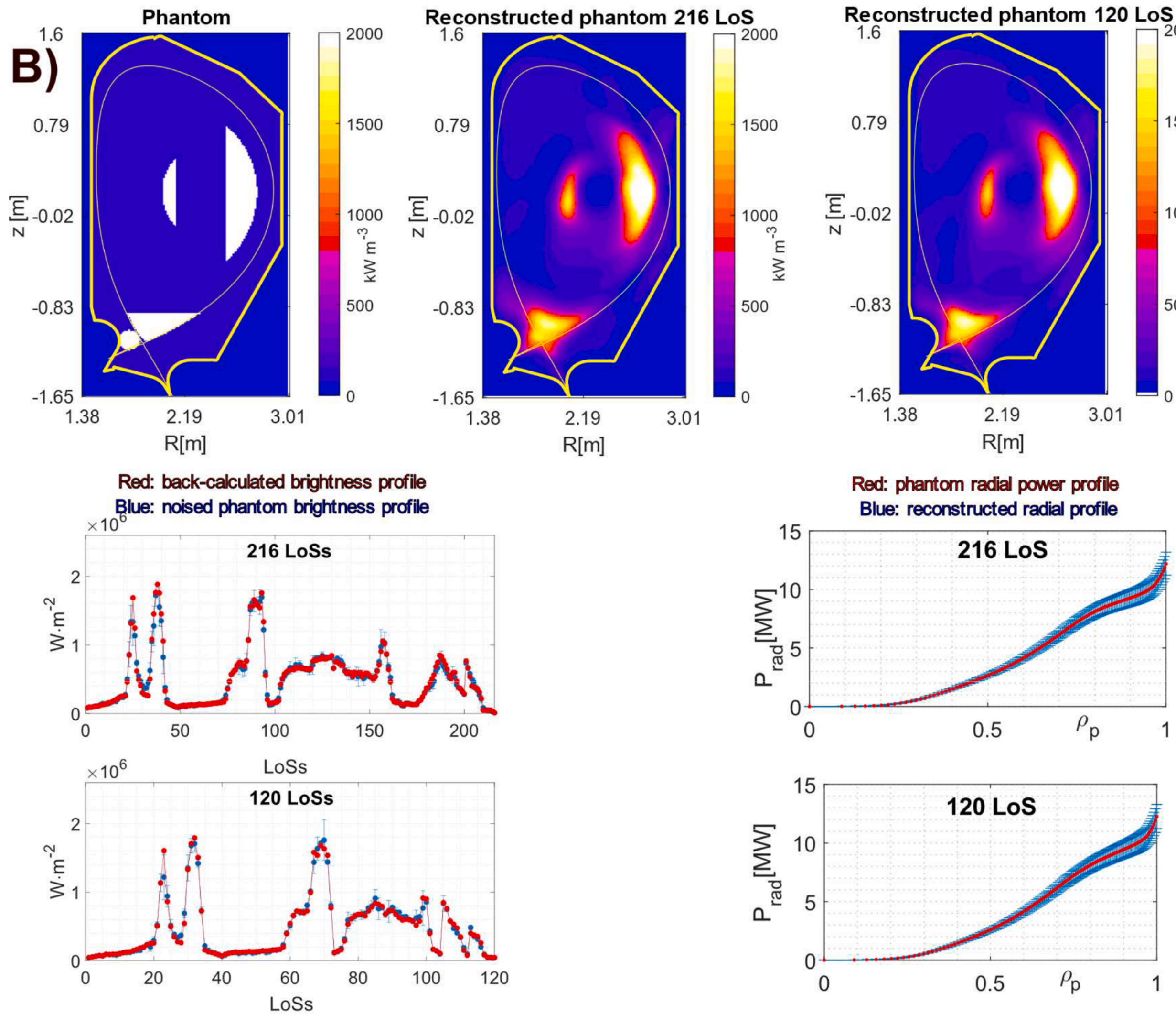

Fig. 5. Second phantom studied, reporting an emissivity profile for a Single Null configuration. b) Inner detached and X-point radiator with impurities accumulating close to the edge and in the core, i.e. leading to a hollow temperature profile. The first row on top shows, from left to right, the created phantom, the reconstructed one using the extended layout (216 LoS) and the one obtained with the reduced one (120 LoS). Second row on the bottom shows, from left to right: the synthetic normally noised brightness profile of the bolometers for the map of emissivity of the phantom (blue) and the back calculated brightness profile (red) for each detector, for both layouts; the radiation profiles up to the LCFS. The error bars are related to the 10 % of normally noised set of projections.

bolometry. Then, a series of engineering solutions are under optimizations, as stated in Section 2, and will be implemented to make these contributions practically negligible. These solutions may include an internal grooving texture for the box, a series of optical stops, including a millimetric grid for ECRH and a TiO_2 or Al_2O_3 coating layer to further reduce both reflections and ECRH stray, as already implemented on AUG and TCV [38,39].

Fig. 3 shows then the cumulative sum of the values of the projection matrix for each pixel for both the extended and the reduced layouts. It is possible to observe brighter pixels corresponding to those both closer and covered from a higher number of LoSs. As mentioned in the commentary to Fig. 2, some characteristics emerge also from Fig. 3 which are the same as in Fig. 1 and in Fig. 2. The reduced layout covers more of the inner top guard limiter and the horizontal arrays in P3 show a lower degree of superposition.

Obviously, the calculations just described make it possible to estimate not only the brightness, but also the incident radiated power on any foil.

Finally, it has been possible to validate the geometrical layout, by using a series of synthetic emissivity profiles, usually called as *phantoms*. The following subsection shows the results obtained with the layouts considered.

4.2. Layout validation

In this subsection five phantoms have been studied in order to verify the actual ability of the previously discussed layouts to reproduce the original emissivity profile, with an appropriate tomographic code. As mentioned in Section 3, the ML has been considered due to its specific advantages and the maturity of its implementation.

The phantoms considered are from now on labelled with the letters A, B, C, D and E and represent quite demanding emissivity profiles. They are shown in Fig. 4(A), Fig. 5(B), Fig. 6(C), Fig. 7(D) and Fig. 8(E) for a Single Null scenario, having then the same magnetic topology as the one shown in Fig. 6 of [11]. Those labelled A, B, C, D show two main regions, a hypothetical radiative region on the low-field side, due to impurity accumulation close to the edge for example, and an inner one to the LCFS, close to the X-point, which has been observed on JET[3,40], and has been recently linked to the so called X-point radiator regime[5]. Then, the phantoms A and B show an inner detached configuration, while the C and D an outer detached one. Phantoms B and D then show a central feature that would experimentally provide a hollow electron

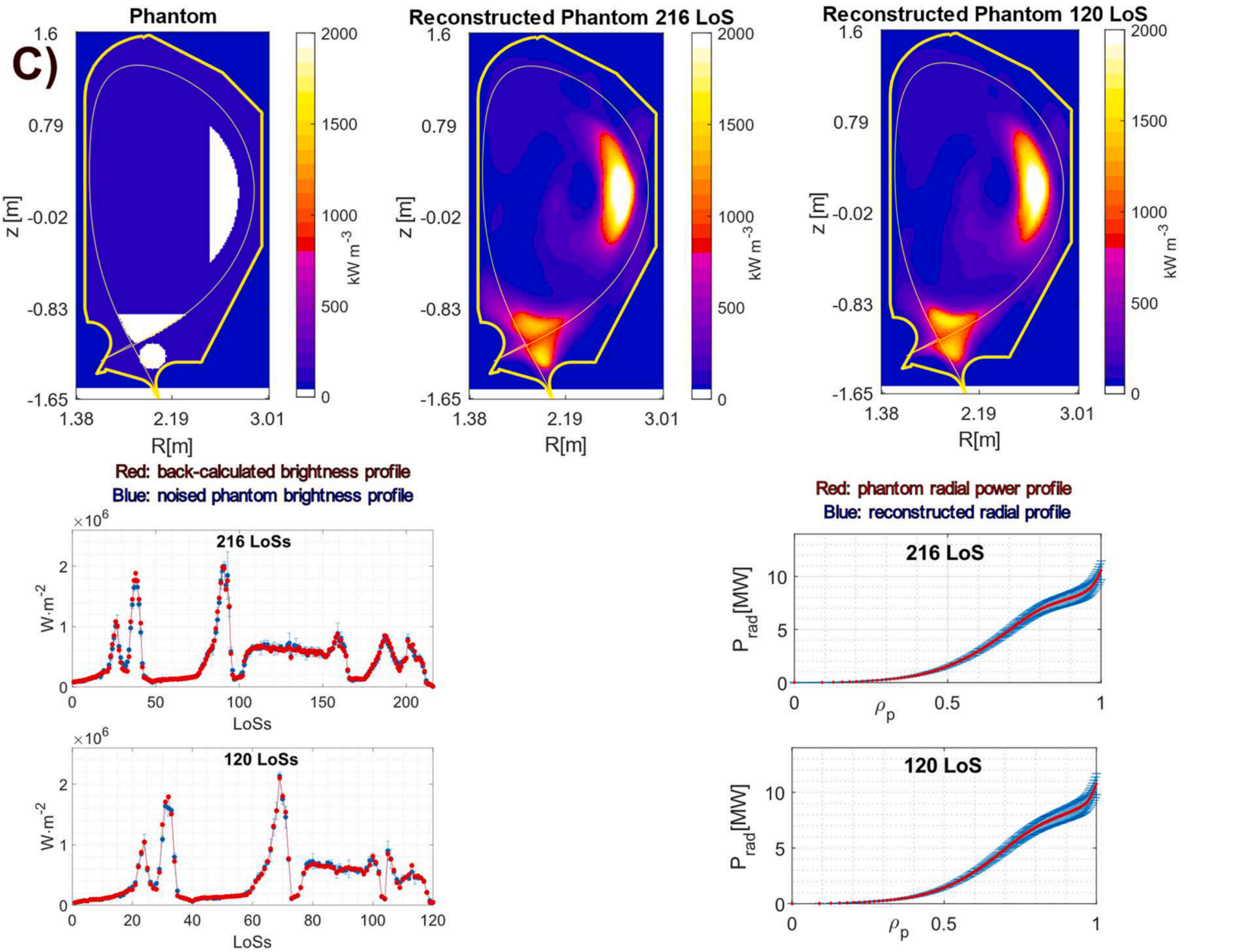

Fig. 6. Third phantom studied, reporting an emissivity profile for a Single Null configuration. c) Outer detached and X-point radiator with an edge accumulation. The first row on top shows, from left to right, the created phantom, the reconstructed one using the extended layout (216 LoS) and the one obtained with the reduced one (120 LoS). Second row on the bottom shows, from left to right: the synthetic normally noised brightness profile of the bolometers for the map of emissivity of the phantom (blue) and the back calculated brightness profile (red) for each detector, for both layouts; the radiation profiles up to the LCFS. The error bars are related to the 10 % of normally noised set of projections.

temperature profile due to accumulated impurities also in the core. This could be confirmed empirically, for example by the SXR. Such minor features, i.e. the detached configurations and the central emissivity, are in principle hidden by the large peripheral features and have been a major source of uncertainties on JET[40,35],. Finally, the phantom E in Fig. 8 is a challenging one in principle and shows the importance of the anisotropic smoothing implemented. In this case the phantom mimics either an ideal radiative mantle for impurity screening or a fast rotating mode trapping impurities.

It should also be noted that each phantom has a background emissivity equal to an arbitrary 5 % of the maximum constructed value of the phantom itself. These phantoms have been studied with the extended layout and the reduced one. In addition, forty-eight copies of the projections of the noise-free phantoms have been created and four groups of twelves have been formed. Then each group has been randomly and normally ($\mathscr{N}_m(\mu = 0, \sigma)$) noised. The standard deviation of the normal distribution used for generating the noise of each group has been set as a percentage of the measurement itself, i.e. $\sigma_m := \{0.05 \cdot I_m, 0.1 \cdot I_m, 0.15 \cdot I_m, 0.2 \cdot I_m\}$.

The radiated powers obtained from the derived tomograms are consistent with those expected and the error estimates are in line with the normal noise added to the projections [41]. The reduced layout generally shows slightly higher errors. Details are given in Tables 2–3 in Appendix A. There, the total radiated power in the vessel (P_{rad}), as well as in the core plasma (P_{core}), i.e. within the LCFS, and the power emitted outside the LCFS (P_{SOL}), are reported. Technically, the latter does not refer only to the Scrape off Layer, since in this case, also the radiated power emitted within the inner, outer and the private flux regions are considered. However, it has been indicated as P_{SOL}, but it should be noted that it considers the divertor contributions, i.e. $P_{SOL} = P_{rad} - P_{core}$.

In the same tables it is possible to read the reason behind the choice of the values of the emissivity profiles in Fig. 4–8. Considering a Phase 1 for DTT with around ~18 MW of external heating, the ones considered reach up to a ~90 % of radiated fraction, which is actually an ideal upper limit to achieve.

5. Conclusions

In this work, a synthetic bolometric diagnostic has been designed and implemented in order to assess the real capability of the bolometric diagnostic designed for DTT. Starting from three geometrical constraints, it has been possible both to optimise the pinhole aperture on a given image plane and then to characterize each LoS with its three-dimensional extension.

Starting from the actual extended diagnostic layout, it was possible to land on a reduced one with about half of the initial LoSs, i.e. 120 with

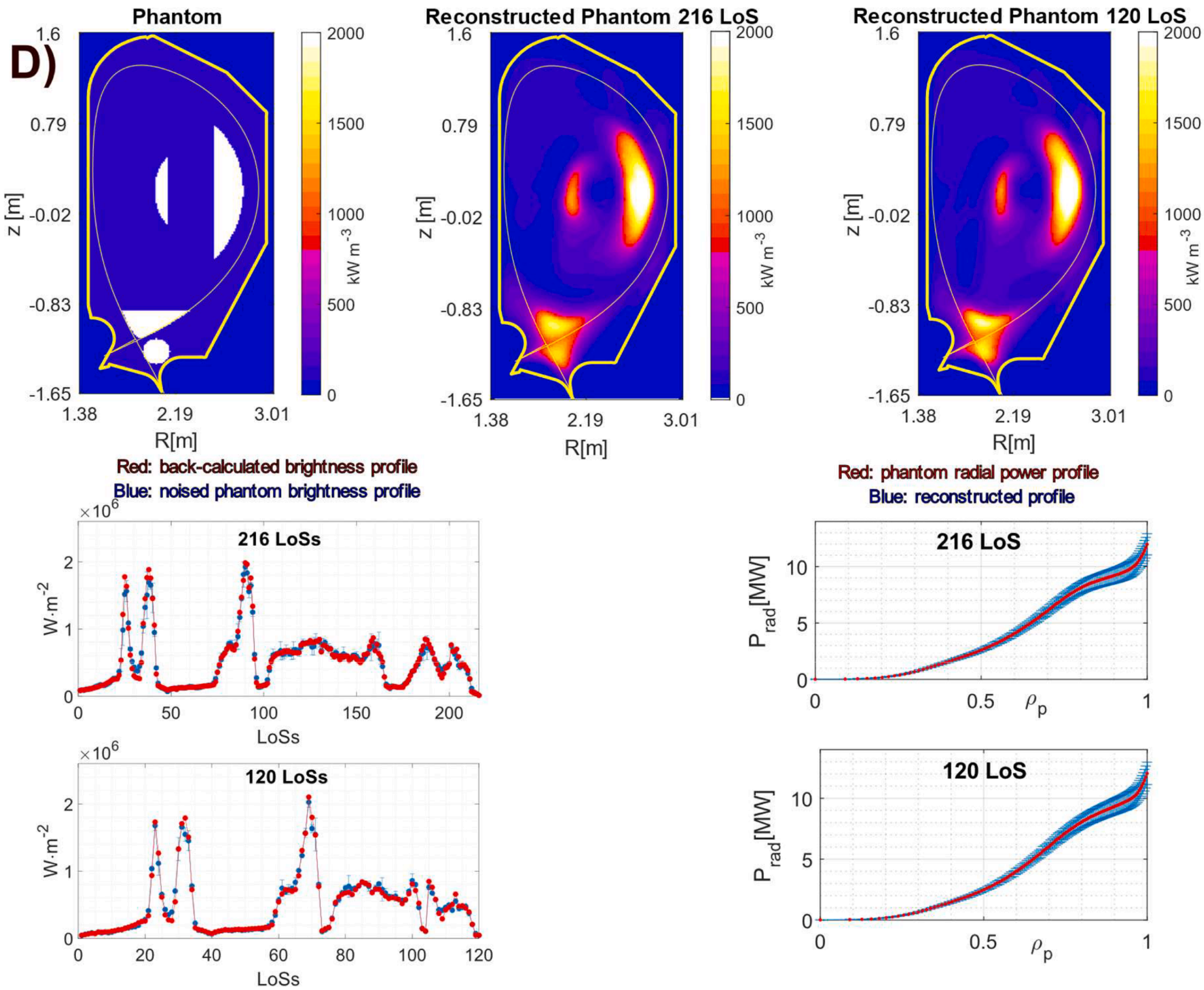

Fig. 7. Fourth phantom studied, reporting an emissivity profile for a Single Null configuration. d) Outer detached and X-point radiator with an edge and a core accumulation, i.e. hollow temperature profile. The first row on top shows, from left to right, the created phantom, the reconstructed one using the extended layout (216 LoS) and the one obtained with the reduced one (120 LoS). Second row on the bottom shows, from left to right: the synthetic normally noised brightness profile of the bolometers for the map of emissivity of the phantom (blue) and the back calculated brightness profile (red) for each detector, for both layouts; the radiation profiles up to the LCFS. The error bars are related to the 10 % of normally noised set of projections.

respect to 216, and to check its ability to reproduce specific and quite challenging emissivity profiles with different normally added noise on the synthetic measurements obtained. In order to carry out such a task, as part of the overall synthetic diagnostic design, the already established ML code, applied to both JET and AUG, was adapted to DTT.

Both the extended and the reduced layouts have been able to reproduce the phantoms and the estimates of the radiated powers with errors in line with the predictions. Finally, also the brightness, e.g. line integrals, has been estimated and consequently, the incident power on each detector can now be evaluated since the etendues are also known.

As a long term goal to fully utilize the data from the diagnostic, efforts are currently being made to optimize the reduced design for real time use of the measured signals. Therefore, once this latter aspect is included in the actual synthetic diagnostic tool[9], it can be expected that the layouts will also be further tested for other scenarios that DTT will consider, such as the negative triangularity one.

It has to be noted that the overall methodology here described can also be applied to other devices, such as the JT60-SA, and of course to other types of line integrated measurements such as SXR signals.

CRediT authorship contribution statement

E. Peluso: Conceptualization, Methodology, Software, Validation, Formal analysis, Investigation, Data curation, Writing – original draft, Writing – review & editing, Visualization. **T. Craciunescu:** Methodology, Software, Data curation, Writing – review & editing. **G.M. Apruzzese:** Validation, Visualization, Writing – review & editing, Project administration. **A. Belpane:** Conceptualization, Validation, Investigation, Writing – review & editing. **S. Palomba:** Data curation, Validation, Project administration. **L. Senni:** Visualization, Data curation, Writing – review & editing. **V. D'Agostino:** Data curation. **M. Gelfusa:** Data curation. **P. Gaudio:** Data curation, Funding acquisition. **L. Boncagni:** Supervision, Funding acquisition.

Declaration of competing interest

The authors declare that they have no known competing financial interests or personal relationships that could have appeared to influence the work reported in this paper.

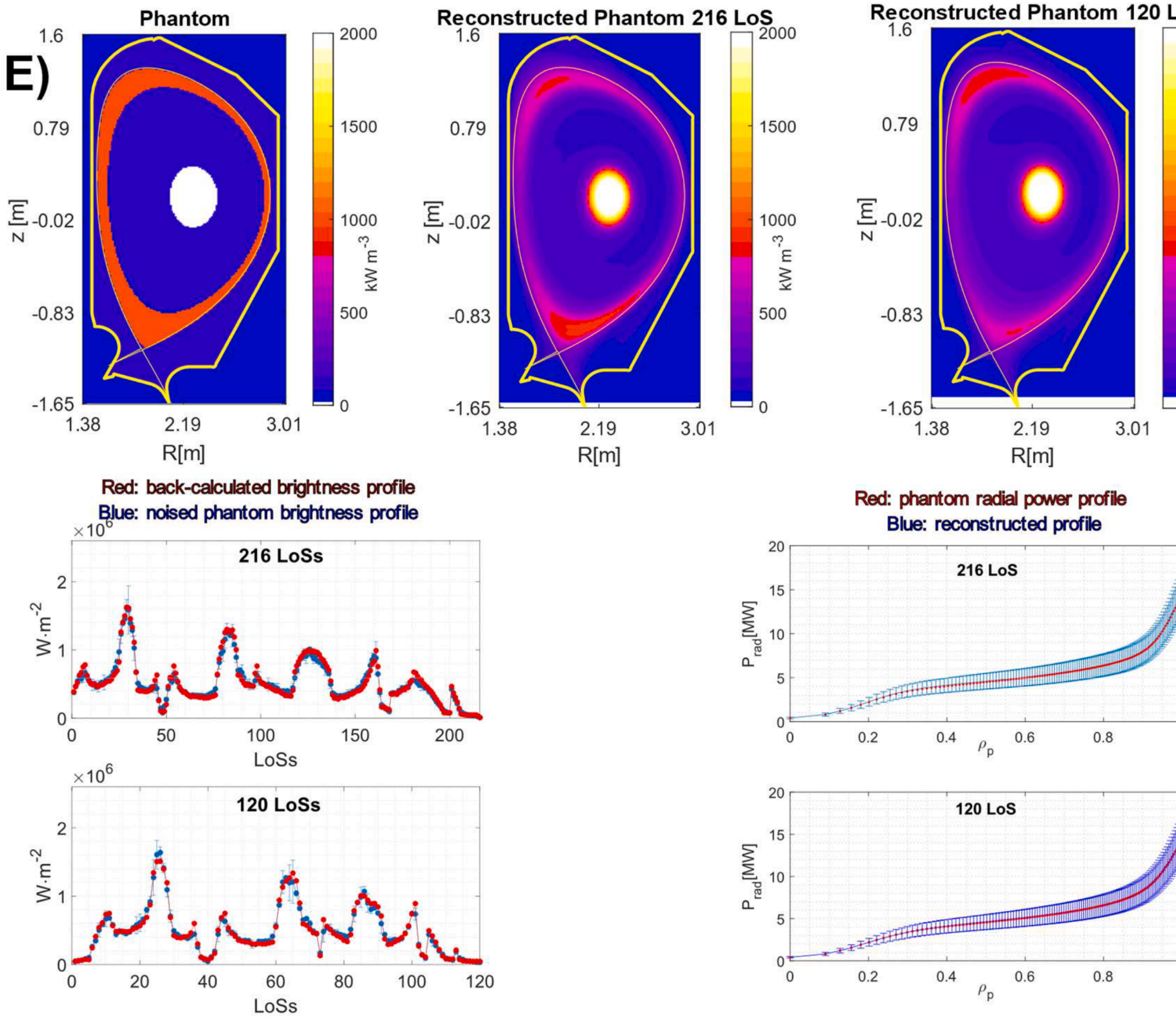

Fig. 8. Fifth and last phantom studied, reporting an emissivity profile for a Single Null configuration. e) Challenging phantom that can be read as a radiative mantle with an impurity screening or a fast rotating mode with trapped impurities. The first row on top shows, from left to right, the created phantom, the reconstructed one using the extended layout (216 LoS) and the one obtained with the reduced one (120 LoS). Second row on the bottom shows, from left to right: the synthetic normally noised brightness profile of the bolometers for the map of emissivity of the phantom (blue) and the back calculated brightness profile (red) for each detector, for both layouts; the radiation profiles up to the LCFS. The error bars are related to the 10 % of normally noised set of projections.

Acknowledgements

Authors are grateful to Antonio Castaldo (ENEA), Lori Gabelleri (DTT), Matteo Iafrati (ENEA), Andrea Murari (CNR) for their suggestions and fruitful interactions.

Appendix A. Estimated radiated power of studied phantoms

Table 2 and Table 3 show the radiated powers discussed in Section 4.2, derived from the reconstructed tomograms of the synthetic emissivity in Fig. 4(A), Fig. 5(B), Fig. 6(C), Fig. 7(D) and Fig. 8(E). The results from both the extended and reduced layouts are shown. For each phantom, the standard deviation of the normal noise added to the measurement, i.e. the line integrals, varies as a percentage of the measurement itself. The total radiated power in the vessel (P_{rad}), as well as in the core plasma (P_{core}), i.e. within the LCFS, and the power emitted outside the LCFS are reported (P_{SOL}). Technically, the latter does not refer only to the Scrape off Layer, since in this case, also the radiated powers emitted within the inner and outer divertor and the private flux region are considered. However, it has been indicated as P_{SOL} i.e. $P_{SOL} = P_{rad} - P_{core}$.

Table 2
Estimates of the radiated power for the phantoms in Fig. 4 (A), Fig. 5(B). Starting from the noise free projections of each phantom, four groups of twelves copies have been considered, Then each set has been normally noised with $\mathcal{N}_m(0,\boldsymbol{\sigma_m} := \{0.05\cdot\boldsymbol{I_m}, 0.1\cdot\boldsymbol{I_m}, 0.15\cdot\boldsymbol{I_m}, 0.2\cdot\boldsymbol{I_m}\})$. $\boldsymbol{P_{rad}}$ stands for the total radiated power in the vessel; $\boldsymbol{P_{core}}$ as the one within the LCFS and $\boldsymbol{P_{SOL}}$ takes into account the radiated power in the scrape off layer and in the divertor region, i.e $\boldsymbol{P_{SOL}} = \boldsymbol{P_{rad}} - \boldsymbol{P_{core}}$.

Phantom [MW]		216 LoS layout			120 LoS layout		
A		$\mathcal{N}_m(\mu = 0, \sigma I)$	$P_{rad} \pm \sigma_{P_{rad}}$ $P_{core} \pm \sigma_{P_{core}}$ $P_{sol} \pm \sigma_{P_{sol}}$ [MW]	Error %	$\mathcal{N}_m(\mu = 0, \sigma I)$	$P_{rad} \pm \sigma_{P_{rad}}$ $P_{core} \pm \sigma_{P_{core}}$ $P_{sol} \pm \sigma_{P_{sol}}$ [MW]	Error %
		$\sigma = 5\%$	13.44 ± 0.61	4.5	$\sigma = 5\%$	13.51 ± 0.75	5.6
			10.96 ± 0.44	4.0		11.07 ± 0.52	4.7
	$P_{rad} = 13.44$		2.48 ± 0.15	6.0		2.44 ± 0.74	8.6
	$P_{core} = 10.98$	$\sigma = 10\%$	13.45 ± 1.43	8.8	$\sigma = 10\%$	13.50 ± 1.36	10.1
	$P_{SOL} = 2.46$		10.95 ± 0.85	7.8		11.07 ± 0.95	8.6
			2.50 ± 0.38	11.9		2.43 ± 0.37	15.3
		$\sigma = 15\%$	13.48 ± 1.82	13.5	$\sigma = 15\%$	13.49 ± 2.21	16.4
			11.00 ± 0.13	12.0		11.04 ± 1.54	14.0
			2.51 ± 0.46	18.2		2.45 ± 0.61	25.1
		$\sigma = 20\%$	13.60 ± 2.50	18.4	$\sigma = 20\%$	13.47 ± 2.60	20.4
			10.06 ± 1.64	16.3		11.04 ± 1.91	17.3
			2.53 ± 0.64	25.2		2.43 ± 0.76	31.5
B		$\sigma = 5\%$	14.57 ± 0.67	4.6	$\sigma = 5\%$	14.62 ± 0.61	4.2
			12.41 ± 0.50	4.0		12.27 ± 0.43	3.5
			2.43 ± 0.17	7.0		2.36 ± 0.17	7.0
		$\sigma = 10\%$	14.62 ± 1.30	8.9	$\sigma = 10\%$	14.63 ± 1.42	9.7
			12.23 ± 0.95	7.8		12.25 ± 0.99	8.1
	$P_{rad} = 14.63$		2.39 ± 0.32	13.5		2.38 ± 0.39	16.2
	$P_{core} = 12.17$	$\sigma = 15\%$	14.56 ± 1.99	13.7	$\sigma = 15\%$	14.53 ± 2.09	14.4
	$P_{SOL} = 2.46$		12.12 ± 1.44	11.9		12.21 ± 1.47	12.0
			2.45 ± 0.50	20.4		2.31 ± 0.57	24.8
		$\sigma = 20\%$	14.61 ± 2.60	17.8	$\sigma = 20\%$	14.65 ± 2.81	19.2
			12.17 ± 1.86	15.3		12.30 ± 2.00	16.3
			2.45 ± 0.65	26.7		2.35 ± 0.75	31.7

Table 3
Estimates for the phantoms in Fig. 6(C), Fig. 7(D) and Fig. 8(E). Starting from the noise free projections of each phantom, four groups of twelves copies have been considered, Then each set has been normally noised with $\mathcal{N}_m(0,\boldsymbol{\sigma_m} := \{0.05\cdot\boldsymbol{I_m}, 0.1\cdot\boldsymbol{I_m}, 0.15\cdot\boldsymbol{I_m}, 0.2\cdot\boldsymbol{I_m}\})$. . $\boldsymbol{P_{rad}}$ stands for the total radiated power in the vessel; $\boldsymbol{P_{core}}$ as the one within the LCFS and $\boldsymbol{P_{SOL}}$ takes into account the radiated power in the scrape off layer and in the divertor region, i.e $\boldsymbol{P_{SOL}} = \boldsymbol{P_{rad}} - \boldsymbol{P_{core}}$.

Phantom [MW]		216 LoS layout			120 LoS layout		
C	$P_{rad} = 13.93$ $P_{core} = 10.72$ $P_{SOL} = 3.20$	$\mathcal{N}_m(\mu = 0, \sigma I)$	$P_{rad} \pm \sigma_{P_{rad}}$ $P_{core} \pm \sigma_{P_{core}}$ $P_{sol} \pm \sigma_{P_{sol}}$ [MW]	Error %	$\mathcal{N}_m(\mu = 0, \sigma I)$	$P_{rad} \pm \sigma_{P_{rad}}$ $P_{core} \pm \sigma_{P_{core}}$ $P_{sol} \pm \sigma_{P_{sol}}$ [MW]	Error %
		$\sigma = 5\%$	13.80 ± 0.63	4.6	$\sigma = 5\%$	13.93 ± 0.68	4.9
			10.54 ± 0.44	4.2		10.72 ± 0.47	4.4
			3.25 ± 0.17	5.1		3.22 ± 0.19	5.8
		$\sigma = 10\%$	13.84 ± 1.19	8.6	$\sigma = 10\%$	13.93 ± 1.30	9.3
			10.61 ± 0.85	8.0		10.70 ± 0.91	8.5
			3.24 ± 0.31	9.7		3.23 ± 0.35	10.9
		$\sigma = 15\%$	13.83 ± 1.78	12.9	$\sigma = 15\%$	13.79 ± 1.99	14.4
			10.59 ± 1.26	11.9		10.57 ± 1.42	13.4
			3.24 ± 0.48	14.7		3.22 ± 0.53	16.4
		$\sigma = 20\%$	13.76 ± 2.35	17.1	$\sigma = 20\%$	14.06 ± 2.54	18.1
			10.45 ± 1.65	15.8		10.85 ± 1.79	16.5
			3.30 ± 0.62	18.7		3.21 ± 0.69	21.6
D	$P_{rad} = 15.03$	$\sigma = 5\%$	15.03 ± 0.61	4.0	$\sigma = 5\%$	15.16 ± 0.67	4.4
	$P_{core} = 11.83$		11.93 ± 0.44	3.7		12.04 ± 0.47	3.9
	$P_{SOL} = 3.20$		3.10 ± 0.15	4.8		3.11 ± 0.17	5.5
		$\sigma = 10\%$	15.03 ± 1.25	8.3	$\sigma = 10\%$	15.12 ± 1.30	8.6
			11.92 ± 0.91	7.6		11.97 ± 0.92	7.7
			3.11 ± 0.31	9.9		3.15 ± 0.35	11.0
		$\sigma = 15\%$	15.02 ± 1.91	12.7	$\sigma = 15\%$	15.13 ± 1.93	12.8
			11.96 ± 1.38	11.5		11.99 ± 1.37	11.4
			3.05 ± 0.48	15.7		3.14 ± 0.51	16.3
		$\sigma = 20\%$	15.09 ± 2.54	16.8	$\sigma = 20\%$	15.23 ± 2.78	18.3
			12.08 ± 1.83	15.2		12.00 ± 1.86	15.5
			3.02 ± 0.63	20.8		3.23 ± 0.71	22.0
E	$P_{rad} = 16.72$	$\sigma = 5\%$	16.72 ± 0.75	4.5	$\sigma = 5\%$	16.42 ± 0.78	4.8
	$P_{core} = 14.90$		14.90 ± 0.65	4.4		14.59 ± 0.67	4.6
	$P_{SOL} = 1.82$		1.822 ± 0.089	4.9		1.81 ± 0.10	5.8
		$\sigma = 10\%$	16.72 ± 1.44	8.6	$\sigma = 10\%$	16.44 ± 1.59	9.7
			14.90 ± 1.23	8.3		14.49 ± 1.34	9.3

(continued on next page)

Table 3 (*continued*)

Phantom [MW]	216 LoS layout			120 LoS layout		
		1.82 ± 0.18	9.5		1.83 ± 0.21	11.5
	$\sigma = 15\%$	16.71 ± 2.17	13.1	$\sigma = 15\%$	16.45 ± 2.40	14.6
		14.89 ± 1.89	12.7		14.63 ± 2.04	14.0
		1.81 ± 0.26	14.6		1.81 ± 0.32	17.6
	$\sigma = 20\%$	16.80 ± 2.99	17.8	$\sigma = 20\%$	16.37 ± 3.19	19.5
		14.99 ± 2.59	17.3		14.52 ± 2.72	18.7
		1.82 ± 0.36	20.1		1.85 ± 0.43	23.0

Data availability

Upon request, the data will be made available once its release has been authorised.

References

[1] K.F. Mast, et al., low noise highly integrated bolometer array for absolute measurement of VUV and soft x radiation, Rev. Sci. Instrum. 62 (1991) 744, https://doi.org/10.1063/1.1142078.

[2] L.C. Ingesson, et al., "Chapter 7 tomography diagnostics: bolometry and soft-x-ray detection, Fus. Sci. Technol. 53 (2008), https://doi.org/10.13182/FST53-528.

[3] M. Bernert, et al., Power exhaust by SOL and pedestal radiation at ASDEX upgrade and JET, Nuclear Mater. Energy 12 (2017) 111–118.

[4] U. Stroth, et al., Model for access and stability of the X-point radiator and the threshold for marfes in tokamak plasmas, Nucl. Fusion 62 (2022) 076008, 16pp.

[5] M. Bernert, et al., The X-point radiating regime at ASDEX upgrade and TCV, Nuclear Mater. Energy 34 (2023) 101376.

[6] G. Pucella, et al., Onset of tearing modes in plasma termination on JET: the role of temperature hollowing and edge cooling, Nucl. Fusion 61 (2021) 046020.

[7] S. Zeng, et al., Magnetic island formation and rotation braking induced by low-Z impurity penetration in an EAST plasma, Nucl. Fusion 63 (2023) 046018.

[8] B. Sieglin, Disruption avoidance and investigation of the H-mode density limit in ASDEX upgrade, Plasma Phys. Control Fusion. 66 (2024) 025004.

[9] Peluso E. et al., "Initial design of a real-time and intershot bolometric data exploitation strategy for DTT", ICFDT7, Frascati 21st-23rd October 2024.

[10] F. Romanelli, et al., Divertor Tokamak Test facility project: status of design and implementation, Nucl. Fusion 64 (2024) 112015, https://doi.org/10.1088/1741-4326/ad5740.

[11] F. Crisanti, et al., Physics basis for the divertor tokamak test facility, Nucl. Fusion 64 (2024) 106040, https://doi.org/10.1088/1741-4326/ad6e06.

[12] G.M. Apruzzese, et al., Progress status of DTT bolometric diagnostic design, in: 49th EPS Conference on Contr. Fusion and Plasma Phys, 3-7 July, Bordeaux, 2023.

[13] G.M. Apruzzese, et al., The updated bolometric diagnostic design for DTT, in: 50th EPS Conference on Contr. Fusion and Plasma Phys, 8-12 July, 2024. P5.043.

[14] R.L. Streit. Poisson Point Processes, Imaging, Tracking and Sensing, Springer, New York Dordrecht Heidelberg London, 2010, https://doi.org/10.1007/978-1-4419-6923-1. ISBN 978-1-4419-6922-4 e-ISBN 978-1-4419-6923-1.

[15] A. Huber, et al., Upgraded bolometer system on JET for improved radiation measurements, Fusion Eng. Des. 82 (2007) 1327–1334, https://doi.org/10.1016/j.fusengdes.2007.03.027.

[16] M. Bernert, et al., Application of AXUV diode detectors at ASDEX upgrade, Rev. Sci. Instrum. 53-3 (2014) 104003.

[17] W. Wan, et al., Progress of the bolometer diagnostic system on EAST, Plasma Sci. Technol. 26 (2024) 095102, 8pp.

[18] V. D'Agostino, et al., Conceptual design of the bolometric camera of DTT: mechanical layout, in: Submitted to Fusion Engineering and Design, 33rd SOFT Conference, Dublin, 2024.

[19] S. Jahanbakhsh, et al., Calibration and thermal test results of prototype bolometer sensors for ITER fusion reactor, Rev. Sci. Instrum. 94 (2023) 033503, https://doi.org/10.1063/5.0134449.

[20] H. Meister, Bolometer sensor holder suitable for ITER-relevant conditions, Fus. Eng. Design 190 (2023) 113503, https://doi.org/10.1016/j.fusengdes.2023.113503.

[21] E. Peluso, et al., Correction of JET bolometric maximum likelihood tomography for local gas puffing, Plasma Phys. Control. Fusion 65 (2023) 075003, https://doi.org/10.1088/1361-6587/accd1c.

[22] A. Belpane, Mechanical design of the new bolometric and soft-X ray diagnostics for DTT", to be submitted to JINST, ICFDT7, Frascati (2024).

[23] J. Baños, et al., Design and line-of sight optimization for VV-mounted and divertor-mounted bolometer cameras in ITER, in: 33rd SOFT, Dublin, Ireland, 2024 (22nd -27th September.

[24] S.R. Deans, The radon transform and some of its applications, Dover, 2007. ISBN: 0486462412.

[25] T. Craciunescu, et al., Maximum likelihood bolometric tomography for the determination of the uncertainties in the radiation emission on JET TOKAMAK, Rev. Sci. Instrum. 89 (5) (2018) 053504, https://doi.org/10.1063/1.5027880, 89053504-1-8.

[26] T. Craciunescu, et al., Maximum likelihood bolometry for ASDEX upgrade experiments, Phys. Scr. 98 (2023) 125603, https://doi.org/10.1088/1402-4896/ad081e.

[27] T. Craciunescu, et al., A comparison of four reconstruction methods for JET neutron and gamma tomography, Nuclear Instrum. Method. Phys. Res. A 605 (2009) 374–383, https://doi.org/10.1016/j.nima.2009.03.224.

[28] L.A. Shepp, Y. Vardi, Maximum likelihood emission tomography, IEEE Transac. Med. Imag. (1982) 113–122. OctoberMI-1, NO. 2.

[29] K. Lange, K. Carson, EM reconstruction algorithms for emission and transmission tomography, J. Compuler Assist. Tomogr. (1984) 306–316.

[30] H.H. Barrett, D.W. Wilson, B.M.W Tsui, Noise properties of the EM algorithm I. Theory, Phys. Med. Biol. 39 (1994) 833–846. E. J Soares et al., "Noise characterization of block iterative reconstruction algorithms: II. Monte Carlo simulations," IEEE Trans. Med. Imaging 24, 112–121 (2005).

[31] Y. Li, Noise propagation for iterative penalized-likelihood image reconstruction based on Fisher information, Phys. Med. Biol. 56 (4) (2011) 1083–1103.

[32] E. Peluso, et al., A comprehensive study of the uncertainties in bolometric tomography on JET using the maximum likelihood method, Rev. Sci. Instrum. 90 (2019) 123502, https://doi.org/10.1063/1.5119441.

[33] D. Tschumperlé, Fast anisotropic smoothing of multi-valued images using curvature-preserving PDE's, Int. J. Comput. Vis. 68 (2006) 65–82.

[34] M.C. Kennedy, Bayesian calibration of computer models, J. Royal Statist. Soc. 63 (2011) 425–464, https://doi.org/10.1111/1467-9868.00294(2001).

[35] E. Peluso, M. Gelfusa, et al., Dealing with artefacts in JET iterative bolometric tomography using masks, Plasma Phys. Control Fusion. 64 (2022) 045013, https://doi.org/10.1088/1361-6587/ac4854 (12pp),.

[36] C. Giroud, A. Meakins, M. Carr, A. Baciero, C. Bertrand, CHERAB spectroscopy modelling framework, Zenodo, V0.1.0, Dataset, http://doi.org/10.5281/zenodo.1206142, 2018.

[37] M. Carr, et al., Description of complex viewing geometries of fusion tomography diagnostics by raytracing, Rev. Sci. Instrum. 89 (2018) 083506, https://doi.org/10.1063/1.5031087.

[38] M. Bernert, Ph.D Thesis, 2013.

[39] U.A. Sheikh, et al., RADCAM—A radiation camera system combining foil bolometers, AXUV diodes, and filtered soft x-ray diodes, Rev. Sci. Instrum. 93 (2022) 113513, https://doi.org/10.1063/5.0095907.

[40] A. Murari, E. Peluso, et al., Investigating the thermal stability of highly radiative discharges on JET with a new tomographic method, Nuclear Fusion 60 (2020) 046030, https://doi.org/10.1088/1741-4326/ab7536, 12pp.

[41] E. Peluso, et al., On the effects of missing chords and systematic errors on a new tomographic method for JET bolometry, Fus. Eng. Design 146 (2019) 2124, https://doi.org/10.1016/j.fusengdes.2019.03.120. –2.